INL/CON-23-70940-Revision-0

Thermal Analysis of the SIRIUS3 Nuclear Propulsion Fuel Calibration Experiment

May 2023

Frederick N Gleicher, Sebastian Schunert, Mark D DeHart, Mustafa Kamel Mohammad Jaradat

Changing the World's Energy Future

INL is a U.S. Department of Energy National Laboratory operated by Battelle Energy Alliance, LLC

INL/CON-23-70940-Revision-0

Thermal Analysis of the SIRIUS3 Nuclear Propulsion Fuel Calibration Experiment

Frederick N Gleicher, Sebastian Schunert, Mark D DeHart, Mustafa Kamel Mohammad Jaradat

May 2023

Idaho National Laboratory
Idaho Falls, Idaho 83415

http://www.inl.gov

Prepared for the
U.S. Department of Energy
Under DOE Idaho Operations Office
Contract DE-AC07-05ID14517

Thermal Analysis of the SIRIUS3 Nuclear Propulsion Fuel Calibration Experiment

Frederick N. Gleicher,* Mustafa K. Jaradat, Sebastian Schunert, and Mark DeHart

*Reactor Physics Methods and Analysis, Idaho National Laboratory, 2525 Freemont Ave., Idaho Falls, ID, 83404, Frederick.Gleicher@inl.gov

To support long space missions, NASA is designing and testing different fuels for nuclear thermal propulsion. These designs encompass ceramic metallic fuels which are to be irradiated in the TREAT reactor to test the fuel's performance. This type of fuel is a ceramic fuel type dispersed in a metallic matrix. A set of experiments named the SIRIUS experiments are designed to test the performance of ceramic metallic fuels under conditions that are intended to be prototypical of mission conditions. These conditions include going from cold conditions (300K) to very hot conditions (2700K-3000K) in a very short amount of time (tens of seconds). The SIRIUS-3 experiment tests a column of 16 fuel specimens under irradiation conditions. For this paper, a Bison model is constructed and thermal analysis of the SIRIUS-3 experiment is performed. These analyses reveal the importance of different local experimental components to characterize the heat transport phenomena of the ceramic metallic fuel. This modeling and analysis also informs predictive modeling for future experiments such as the SIRIUS-2C and SIRIUS-5 tests, which will be a ceramic fuel type dispersed in a ceramic matrix.

I INTRODUCTION

NASA is considering Nuclear Thermal Propulsion (NTP) for long range extraterrestrial missions; these engines eject hot hydrogen gas heated by a nuclear reactor for rocket thrust [1]. To economize the use of hydrogen to the greatest extent possible, the NTP engines will be expected to, in a very short time (i.e., on the order of a minute or less), go from cold($\sim 300K$) zero power conditions to full operational power, with a coolant outlet temperature on the order of 2700–3000 K [2]. These conditions will introduce significant thermomechanical stresses on the NTP fuel. The objective of the SIRIUS series of experiments is to examine the performance of candidate NTP fuel materials when subjected to temperature ramp rates that are prototypical of NTP system startup and operation. The experiments will be accomplished by executing a series of shaped transients within the Transient Reactor Test Facility (TREAT) on the SIRIUS specimens, while collecting in situ specimen temperature data. A shaped transient in TREAT is the computer-controlled, control rod driven maintenance of the reactor power to produce a desired temperature in the target specimen. These tests will determine whether operational startup ramps and peak temperatures will result in detrimental fuel performance phenomena (i.e. fuel deformation, fragmentation and cracking).

To this end, INL has been evaluating a number of SIRIUS experiments; these evaluations include thermal analysis of the SIRIUS experiments [3] with the fuel performance tool Bison [4]. This paper begins with a brief experiment overview of fuel sample and experiment configuration followed by the developed Bison finite element model. That section is followed by a set of results with a brief discussion, and finally the paper concludes with suggestions for future work.

II SIRIUS-3 EXPERIMENT DESCRIPTION

This section describes the SIRIUS-3 fuel specimen stack, the flask which contains the specimen stack and the capsule that contains the flask. The capsule, which has a top Conax and an outlet gas valve at the bottom, contains a static cover gas mixture of Ar ($97wt\%$) and H_2 ($3wt\%$) that surrounds both the flask and the experiment fuel element specimens. The capsule is composed of a nickel-copper alloy for the lower half of the capsule and Inconel for the upper half. and is similar to the one used for the earlier SIRIUS-2 experiments [5]. The upper capsule portion remains unchanged from the previous design while the lower capsule portion has been modified to accommodate the longer specimen stack, rather than the single hexagonal specimen of SIRIUS-2. The length of the bottom capsule is extended should the full stack of specimens melt and the molten fuel material relocate into the heat sink. The capsule is placed within the Minimal Activation Retrievable Capsule Holder (MARCH) and the capsule holder is placed within the Broad Use Specimen Transient Experiment Rig (BUSTER). Details for both MARCH and BUSTER are given in reference [6].

The SIRIUS-3 experiment is composed of sixteen stacked specimen elements [7]; Figure 1 shows a diagram of the specimen element with labels of the different components. From the diagram, the specimen stack is bounded by two retainer caps which are made of molybdenum, and seven molybdenum element tubes thread each of the bore holes in the fuel element specimen. Inner holes with small tooth-like protuberances are in the retainer cap and friction-grip the molybdenum element tubes to hold them in place. A rendering of the retainer caps are shown in Figure 2, and the dimensions of the retainer caps and molybdenum element tubes are given in Table I.

TABLE I. Table of dimensions for both the Retainer Cap and Element Tubes

Parameter	Value
Outer Retainer Cap Diameter [cm]	1.651
Inner Retainer Hole Diameter [cm]	0.2870
No. Holes	7
Retainer Cap Height [cm]	0.0127
Element Height [cm]	20.739
Element Tube Outer Diameter [cm]	0.3023
Element Tube Inner Diameter [cm]	0.2438

Figure 3 shows the a single fuel element with the seven bore holes. The dimensions for a single specimen are given in Table II. The composition of each specimen is a ceramic metallic fuel (CERMET) composed of Uranium Nitrite, Molybde-

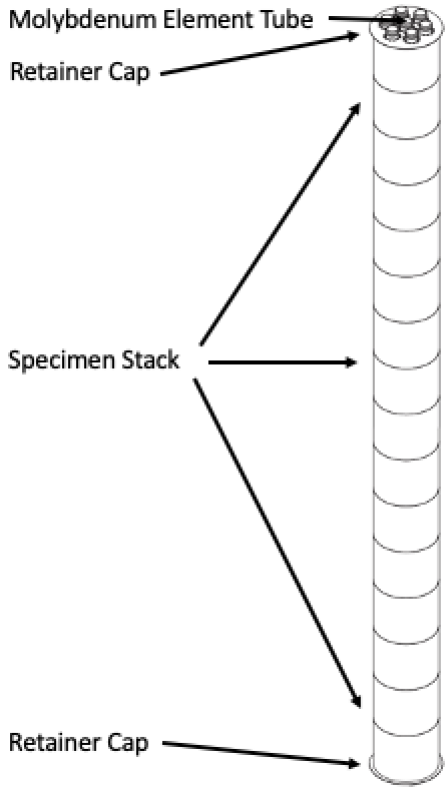

Fig. 1. SIRIUS-3 Specimen Element Stack Diagram

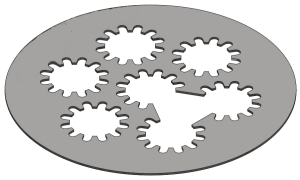

Fig. 2. A three dimensional rendering of the Retainer Cap

Fig. 3. Three-dimensional rendering of a single SIRIUS-3 fuel specimen

TABLE II. Table of pellet dimensions and parameters

Parameter	Value
Outer Sample Diameter [cm]	1.4757
Bore Hole Diameter [cm]	0.3124
No. Bore Holes	7
Height [cm]	1.27
Single Sample Volume [cm^3]	1.4908
Single Sample Outer Area [cm^2]	5.8879
Total number of Fuel Specimens	16

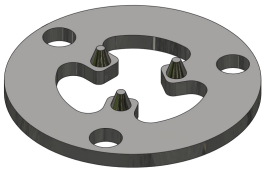

Fig. 4. Three dimensional rendering of the Hold-Down Ring

num, and Tungsten. The fuel specimen element composition are given in Table III, and were taken from Ref. [8].

TABLE III. Table of pellet composition

Parameter	Value
Density [g/cm^3]	12.015
UN [$wt\%$]	64.38
W [$wt\%$]	10.69
Mo [$wt\%$]	24.93
U-235 Enrichment [$wt\%$]	20.93

To hold the experiment in place tungsten hold-down rings are positioned and below the retainer caps, and a 3D render of the hold-down ring is shown in Fig. 4. The rings also have three holes for the tungsten stand off rods that help keep the experiment in place, and the rods connect to the bottom heat sink.

The flask container consists of a flask wall, six flask studs and three standoff rods that surrounds the fuel element experiment. The flask studs are located in grooves in the flask wall, and the three standoff rods are between the flask wall and the fuel element stack. Below the flask is a molybdenum heat sink with a hole to catch the experiment if the specimens should melt. Above the flask walls is a flask cap which is composed of an Inconel alloy and has a top ring and three hanger rods. As stated tungsten hold-down rings sandwich the molybdenum retainer caps, and have slots for the standoff rods. Springs surround the standoff rods above and below the respective hold-down ring and help hold the fuel specimen elements in place for the flask. Each hold-down ring is threaded by a standoff rod and the stand off rods are surrounded by springs. Figure 5 shows a diagram and the flask.

III SIRIUS-3 CALIBRATION IRRADIATION DESCRIPTION

For the SIRIUS-3 series of irradations a calibration irradiation is first performed followed by other higher power

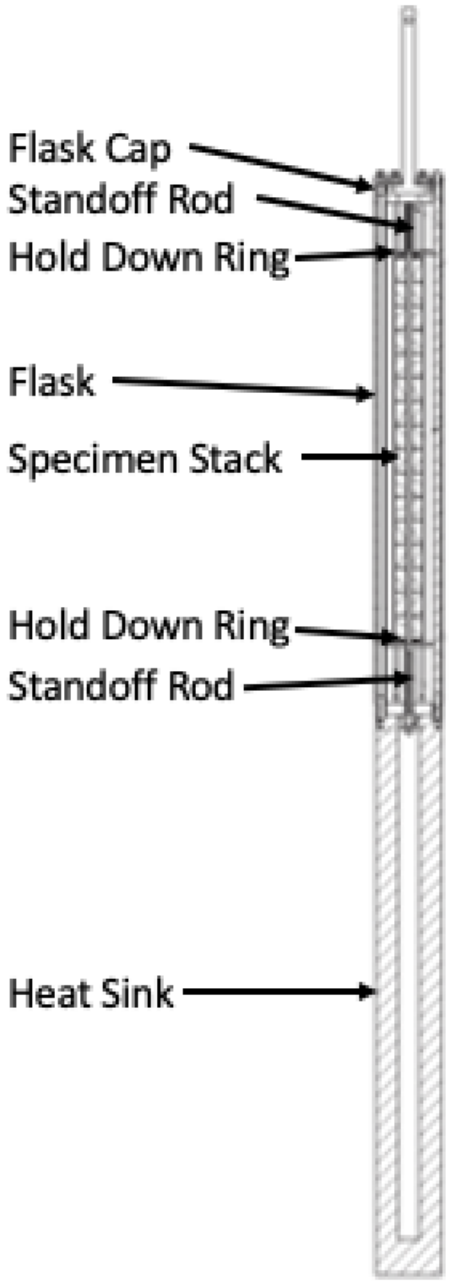

Fig. 5. SIRIUS-3 Flask Assembly Diagrams with labels for different elements

irradiations. The calibration irradiation is used to check the working order of the instrumentation and to determine calibration factors. A calibration factor is a factor that relates core energy release to induced energy deposition in fissile bearing material specimens during a TREAT irradiation. For components that do not have fission bearing material heat generation rates are computed for neutron and proton energy deposition. For the SIRIUS-3 Calibration run the TREAT reactor is pulsed, the TREAT reactor transient rods are removed from the core and TREAT operates in *natural transient* mode to produce a spike like shape in reactor power, with the control rods inserted back into the core between 24 s to 25 s to terminate the transient. Figure 6 shows the measured reactor power in blue.

Thermocouples are located in the fuel stack and the flask to measure temperature data. A thermocouple was positioned at the axial midplane of the fuel stack, and a second thermocouple was placed at the top of the stack; both were attached to the outer surface of the fuel specimens. Another thermocouple was positioned at the top of the flask to measure the flask wall temperature. Plots of the axial midplane temperature and the TREAT reactor power for the SIRIUS-3 calibration are shown in Figure 6. For this figure, the ordinate for the temperature is given on the left and the ordinate for the power is shown on the right.

In addition, a plot of the temperature measurement of midplane and top and the measurement temperature of the flask is shown in Figure 7. In Figure 7 the left ordinates are the temperature measurements for the midplane and top and the right ordinate is the flask temperature measurement. Figures 6 and 7 show that the local specimen temperatures reach a peak after immediate insertion of the TREAT reactor control rods and the power is reduced to effectively zero. The specimen temperatures then decrease as they cool down.

However, the flask temperature shown in Figure 7 shows an increase in temperature as the TREAT transient is terminated. This increase is due to the thermal radiation heating from the specimen as the the fuel element specimens cool down.

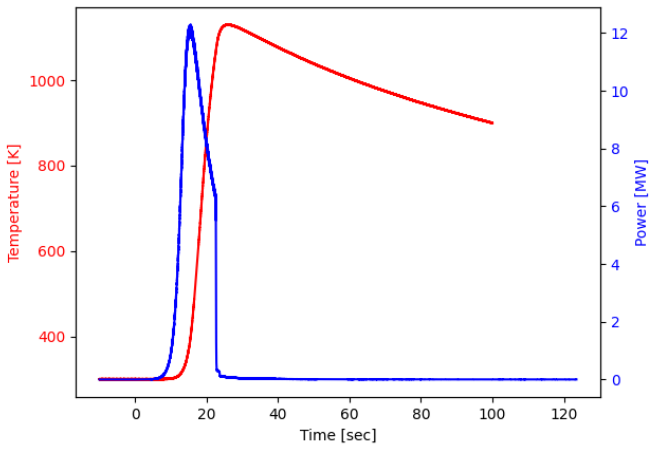

Fig. 6. SIRIUS-3 Power and Outer Mid-Height Thermocouple Temperature

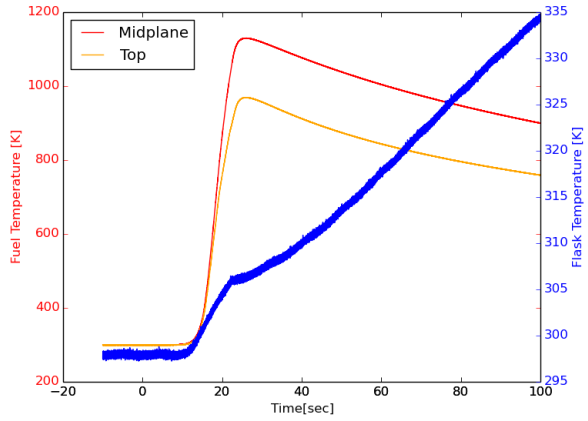

Fig. 7. SIRIUS-3 Thermocouple Measurement Temperatures

IV BISON SIRIUS-3 THERMAL MODEL

In this section the thermal Bison finite element model (FEM) is described. To make the BISON FEM tractable and aid in the deduction of the dominant thermal physics for the given measurements, a number of simplifications are made to the FEM. An center axial sliced view of the simplified FEM is shown in Figure 8, and a radial sliced view of the BISON FEM is shown in Figure 9. The Bison FEM simplifications are the omission of the stand off rods, the flask stud rods, and components outside of the flask, and component simplifications of the retainer cap, molybdenum element tubes, and the hold-down ring. The Bison FEM consists of the sixteen fuel specimen elements, the molybdenum element tubes, the simplified top and bottom retainer rings, simplified hold-down rings, and the outer flask.

As shown in Figures 8 and 9, the retainer caps and hold-down rings are simplified to be cylindrical plates with holes for the molybdenum tube and are assumed to be in contact with each other. The molybdenum element tubes that occupy the cooling channels in the fuel specimen elements are assumed to be perfectly centered and are not in contact with the fuel element specimens. The notching that provides contact to the retainer rings for the molybdenum element tubes is omitted. The dimensions of the different components are given in Table IV.

TABLE IV. Table of component dimensions

Component	Inner Diameter [cm]	Outer Diameter [cm]	Height [cm]
Specimen	0.3124	1.4757	1.27
Element Tube	0.2807	0.30226	20.74
Flask	2.8575	3.683	20.32
Retainer Ring	0.3124	1.651	0.0127
Hold-Down Ring	0.3124	2.54	0.16

Also, the flask and fuel stack are assumed to be of the same height, and the specimen density is taken from the ref-

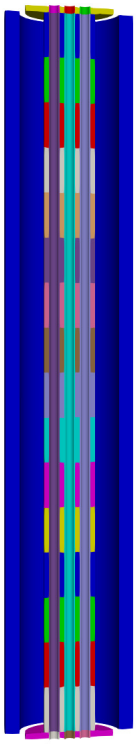

Fig. 8. Diagram of the SIRIUS-3 Bison Thermal Model an axial sliced view

Fig. 9. Diagram of the SIRIUS-3 Bison Thermal Model a radial slice view

erence [9]. Thermal material properties for the fuel element specimens are supplied by Bison, and for non-fuel components the material properties are taken from Reference [10]. For the Bison FEM, different components can be omitted to help show the relevance and impact of a component's absence.

The outer boundary of the flask is set to a constant 300K by applying a Dirichlet boundary condition, and the inner flask surface is set to be in radiating heat exchange between the flask inner boundary the outer fuel element specimen boundary. The radiation heat exchange is performed through a non-meshed region between the inner flask and the outer fuel specimen; thermal contact radiation boundary models are applied. Details for these modeling approaches are discussed in Ref. [4]. The Bison thermal contact model is applied to the outer surface of the molybdenum element tubes and the inner surface of the fuel specimen cooling channels. The inner surface of the molybdenum element tubes are set to an adiabatic boundary condition, and the retainer cap and the hold-down ring have a surface radiation boundary condition applied with a gas temperature of 300K. For the retainer cap and hold-down ring a radiative boundary condition for radiation emission and exchange with the local static gas is applied.

Since the hold-down ring is connected to other components such as the stud rods, these extra components will also thermally conduct and radiate heat during the transient. As described above the hold-down ring has simplified, and rather than introduce more model complexity, a larger emissivity was assigned to the hold-down ring component. A larger emissivity assigned the hold-down ring is expected to help in energy dissipation given that hold-down ring is simplified and many thermally conducting elements are omitted in the model. The emissivities of the different surfaces for the boundaries are given in Table V.

TABLE V. Table of Emissivities for different surfaces

Surface	Emissivity
Inner Specimen Bore Hole	0.8
Outer Specimen	0.8
Inner Flask	0.35
Outer Hold-Down Ring	1.0
Inner Hold-Down Ring	1.0
Outer Element Tube	0.4

In Table V the hold-down ring emissivity is assigned a value of 1.0 to increase heat removal by thermal radiation, and the Inner Specimen Bore Hole and Outer Specimen are assigned a value of 0.8 which is similar to those given in Ref. [3]. The outer element tube is assigned a rough value of 0.4, and the inner flask is assigned a value of 0.35. The inner flask emissivity value of 0.35 is higher than that of molybdenum traditionally around 0.1. The higher emissivity is assigned higher since the thermal radiative transfer occurs with many different components, such as the stud rods, that were omitted to make the Bison FEM tractable. Thus the inner flask emissivity represents an effective radiative transfer between the fuel specimens and the different omitted components and flask. Furthermore, a uniform power density is assigned to each fuel element specimen. For the calculations, the time dependant TREAT power shown in Figure 6 is read by Bison as a comma separated value (csv) file. The power is then converted into a uniform power density by multiplying the TREAT power by the calibration factor and the fuel element specimen density. Details for the calculation of the calibration factors are given by the reference [7]. Calculated values are reproduced in Table VI.

TABLE VI. Table of calibration factors for the different pellets

Specimen ID	Calibration Factor [W/g-MW]
1	2.35
2	2.21
3	2.18
4	2.17
5	2.21
6	2.22
7	2.24
8	2.24
9	2.20
10	2.24
11	2.25
12	2.23
13	2.21
14	2.24
15	2.33
16	2.41

We do observe that the calibration factors listed in Table VI are obtained with a slightly different material density and composition than the one provide in thermal analysis reference [9], and that the calibration factors are assumed to be independent of fuel element specimen temperature. For the stack listing Specimen ID 16 is the top specimen and Specimen ID 1 is the bottom specimen.

V RESULTS

This section discusses the results obtained from an energy budget analysis and the results from the calculations with the FEM thermal model. The energy analysis examines the energy generation, accumulation, and loss mechanics from the experimental temperature data shown in Figure 7, and provides insight into which components need to be modeled and what the potential emissivities are for the different components.

In addition, further analysis is done for the coupling factors and to verify the results listed in Reference [7]. The FEM calculations are compared to measured data and show the importance of the presence of different components on the thermal solution.

V.A Energy Budget Analysis

An initial Bison FEM was constructed with assumed cooling mechanisms such as convection boundary conditions at the fuel specimen boundary, and without adjoining components such as the molybdenum tubes. But the initial model produced temperatures for the center fuel specimen that were too large and did not capture the cool down behavior sufficiently

when compared to the measured temperatures after the reactor shutdown. To help correct the disagreement between the Bison FEM and measured results, an energy budget analysis is performed to understand and identify the important thermal physical mechanisms that lead to the measured temperature curve during both the power transient and the subsequent cool down of the fuel samples. For this analysis, a very simple lumped thermal energy model is proposed

$$\rho c_p V \frac{dT}{dt} = -A\sigma\epsilon_{\text{eff}}(T^4 - T_b^4) + \rho V C_f Q. \quad (1)$$

where ρ is the density of the fuel, V is the volume of the fuel specimen, c_p is the heat capacity of the fuel, T is the measured fuel temperature, T_b is the background or ultimate heat sink temperature set at 300 K, t is time, A is the outer area of the fuel specimen, ϵ_{eff} is the effective emissivity that is defined later, σ is the Stefan-Boltzmann constant, $C_f$is the coupling factor and Q is the power source given by the profile shown in Figure 6. In Eq. 1 the first term is the energy change or accumulation term of a the fuel specimen, the second term represents the thermal irradiation out of the fuel specimen, and the third term is the local energy generation. For the analysis the energy deposition by the TREAT reactor, the subsequent cool down, the effective emissivities due to the cylindrical geometry are all examined. The formula for the effective emissivity is found in Reference [11] and is given by the expression:

$$\epsilon_{\text{eff}} = \frac{1}{\frac{1}{\epsilon_1} + \frac{R_1}{R_2}\frac{1-\epsilon_2}{\epsilon_2}} \quad (2)$$

.

In Equation 2 ϵ_{eff} is the effective emissivity, ϵ_1 is the emissivity of the fuel pellet, ϵ_2 is the emissivity of the flask wall, R_1 is the radius of the fuel pellet, and R_2 is the inner radius of the flask. A plot of Equation 2 is shown in Figure 10 below. In Figure 10, $\epsilon_{\text{eff}}$is the effective emissivity and is

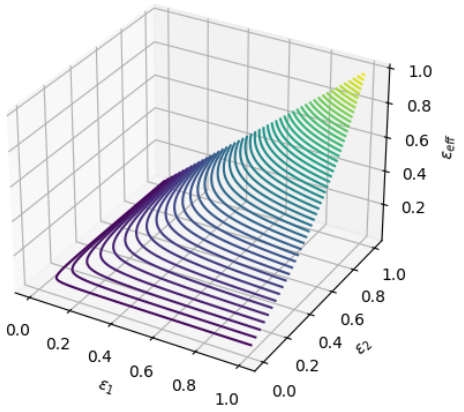

Fig. 10. Emissivity Plot for Concentric Cylinders

shown as a function of the emissivity of the fuel ϵ_1 and the emissivity of the inner flask ϵ_2. In Figure 10 the effective emissivity remains low when the fuel emissivity is low but can become much greater when the fuel emissivity is closer to 1.0. The effective emissivity is also a function of the flask emissivity and increases when the flask emissivity increases. But the maximum effective emissivity is strongly dependent on the value of the fuel emissivity.

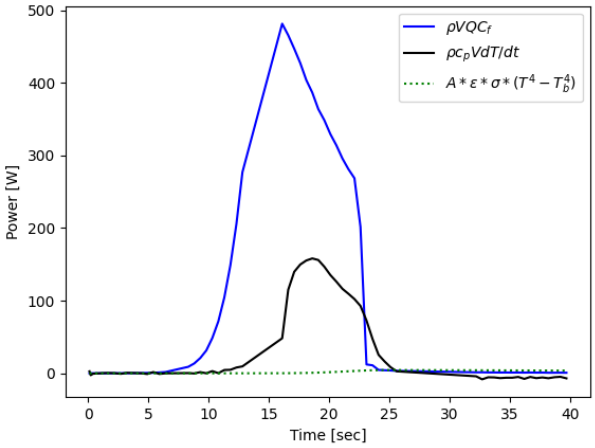

Fig. 11. SIRIUS-3 Energy Analysis

Figure 11 shows the computed quantity of energy generated by a source, the total change or accumulation of energy, and the release of energy due to thermal radiation. The source term in Figure 11 is ρVQC_f is larger than the accumulation term $\rho c_p VdT/dt$, the radiation emission term $A * \epsilon * \sigma * (T^4 - T_f^4)$, and even the sum of both. Figure 11 shows that the energy generated by the fuel far exceeds the energy that is accumulated in the temperature change and the energy that is lost due to radiation. Thus the energy must be transferred away by some other mechanism such as conduction to the molybdenum element tubes, the retainer caps, and the hold-down rings.

The plots in Figures 12 and 13 shows the calculated energy due to thermal radiation with different levels of emissivity of both the inner flask and the central fuel element specimen, and the calculated energy change observed from the cool down of the fuel element after irradiation. Figures 12 and. 13 show the calculated energy after the reactor shutdown and during the monitored cooling of the fuel specimen. This removes the energy source term in Eq. 1. In both plots the calculated thermal radiation energy with the flask emissivity set to $\epsilon_2 = 0.15$ produces results give good agreement with the calculated energy change. The agreement indicates that thermal radiation is a strong candidate for cooling after the fuel specimen is heated, and because of the short duration of the calibration heating other mechanisms for cooling such as gas convection are neglected.

However, other components such as molybdenum element tube, retainer caps, and hold-down rings etc. are not present in the lumped model and have an effect on the fuel specimen local accumulation energy, and must be taken into account for an accurate radiative transfer model. But because the calculated thermal radiation energy gives good agreement with the

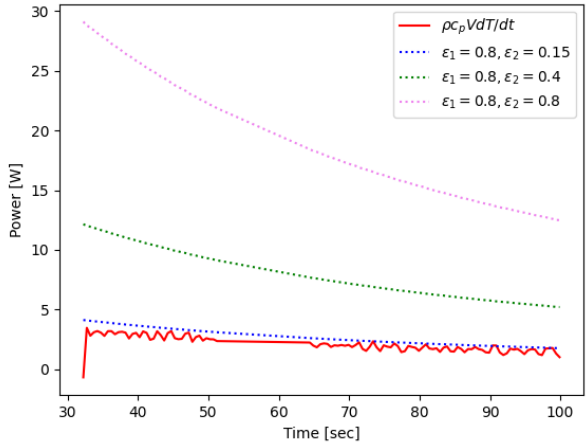

Fig. 12. The SIRIUS-3 central pellet decay profiles for different ϵ_{eff}, and the fuel specimen ϵ_1 is 0.8

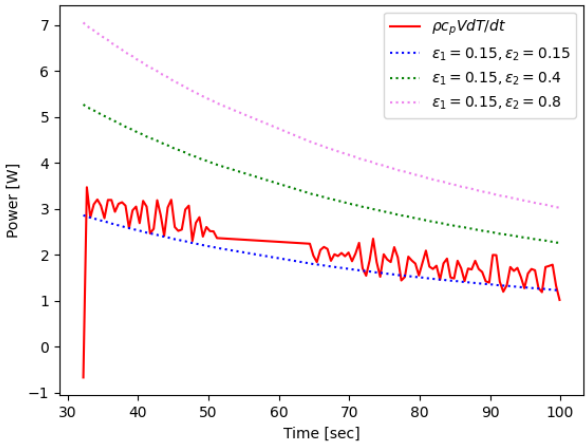

Fig. 13. The SIRIUS-3 central pellet decay profiles for different ϵ_{eff}, and the fuel specimen ϵ_1 is 0.15

calculated energy change, thermal radiation is concluded to be a very a good candidate for the energy loss mechanism during the cool down phase of the experiment, but the modeling of other components such as the molybdenum tubes are clearly necessary to obtain good agreement with measurement.

V.B Calibration Factors

For the SIRIUS-3 thermal analysis the calibration factors are recalculated to verify the magnitude of the calibration factors and to help gauge the effect of the calibration factors on the temperatures of the fuel element specimen. The MCNP calculation results are shown in Table VII; Serpent calculation results are given in Table VIII, and the listed calibration factors from reference [7] are given in Table VI. The units for the values given in Tables VII and VIII for both the calibration factors and the associated σ are[W/g-MW].

The columns labeled 180 MeV/Fission and 200 MeV/Fission are calculated from the model used in reference [7] and assign a value of either 180 MeV or 200 MeV per fission respectively. The calibration factors given in Table IV and 200 MeV/Fission in Table VII should be within an acceptable Monte Carlo error since they have the same assumed local energy deposition per fission. For these two columns the calibration factors are under 4% maximum error and are accepted to be within the given Monte Carlo error. The column Serpent are calibration factors calculated with the Serpent model of the SIRIUS-3 experiment.

In reference [7] a historical value of 182 MeV per fission is applied in the conversion factor for the calculation of the calibration factors. The lower value suggests that in the past a lower amount of energy deposited from fission is thought to occur, and calibration factors have been shown to dynamically change as shown in reference [12]. Thus for investigation calculations with 180 MeV per fission are performed to to obtain lower bound for calibration factors. Here 180 MeV per fission assumes that energy captured from the collision of the fission fragments, fission neutrons and prompt gamma rays as shown in reference [13]. Normalized standard deviations are given in the MCNP σ and Serpent σ columns for the MCNP and Serpent calculations. The standard deviation for MCNP σ applies to the 180 MeV and 200 MeV per fission calculations, and the standard deviation for the results Table VI in the column are not given.

From the calibration factor results the Serpent and 200 MeV/Fission are close to that of the listed model. The calibration factor results from the 180 MeV/Fission are lower as expected since less energy is assumed to be deposited locally from fission. For these results the fuel element specimen density and composition are taken from Reference [7].

V.C Component Analysis on Fuel Element Specimen Temperature

This section covers the temperatures obtained with the Bison FEM and the comparisons to the measurement data. The measurement temperature at the axial mid-height shown in Figure 7 and the results obtained from different Bison calculations are given in Figure 14. The solution labeled "Experiment"

TABLE VII. Table of MCNP coupling factors for the different pellets

Specimen ID	180 MeV per Fission	200 MeV per Fission	MCNP σ
1	2.11	2.34	0.0118
2	2.01	2.24	0.0122
3	1.98	2.21	0.0123
4	1.96	2.18	0.0123
5	1.97	2.19	0.0123
6	2.00	2.22	0.0122
7	1.95	2.17	0.0122
8	2.01	2.23	0.0122
9	2.02	2.24	0.0123
10	1.96	2.18	0.0121
11	2.04	2.27	0.0124
12	2.00	2.27	0.012
13	2.00	2.22	0.0122
14	2.04	2.26	0.012
15	2.04	2.29	0.012
16	2.22	2.47	0.0117

TABLE VIII. Table of Serpent coupling factors for the different pellets

Specimen ID	Serpent	Serpent σ
1	2.39	0.0383
2	2.25	0.0429
3	2.26	0.0449
4	2.22	0.0463
5	2.25	0.0442
6	2.31	0.0415
7	2.21	0.0464
8	2.27	0.0430
9	2.26	0.0421
10	2.25	0.0441
11	2.27	0.0439
12	2.22	0.0428
13	2.31	0.0415
14	2.25	0.0440
15	2.24	0.0446
16	2.42	0.0397

is the outer mid-height temperature obtained from the thermocouple shown in Figure 7, and the solutions labeled Case 1, Case 2, and Case 3 are different models with an increasing number of experimental components present in the Bison model. The labels for these are

- Case 1: The calculation with only the fuel specimens and flask modeled.
- Case 2: The calculation with the fuel specimens, flask, and inner molybdenum tubes. The molybdenum tubes are positioned through the fuel specimens.
- Case 3: The calculation with the fuel specimens, the outer flask, the inner molybdenum tubes, the retainer caps and the hold-down rings.

Figure 14 shows that for the outer mid-height temperature the presence and modeling of molybdenum rods helps to capture a better temperature solution than without. Initially during the transient local thermal conduction heats up the molybdenum rods and then after the reactor is shut down the molybdenum rods provide a local heat source that provides energy to the fuel specimen. Although the molybdenum rods are hollow the inner diameter of the rods is small, and the rods approach the temperature of the fuel specimen during the transient Since Case 1 has no molybdenum rods through the fuel specimens, the extra energy source obtained through thermal conduction of the molybdenum rods is not present, and thus the temperature shows a greater decrease as the mid-height fuel specimen cools. Also in Figure 14 Case 3 and Case 2 are close which suggests that for the mid-height energy dynamics is localized. Any approximations and omissions of the top and bottom hold-down rings or retainer caps does not have an effect on the outer mid-height temperature. The difference between the experiment measurement and the different cases are possibly due to differences between the location of the thermocouple and the location and manner of how the Bison model's result are computed (e.g., surface average, point value, volume average).

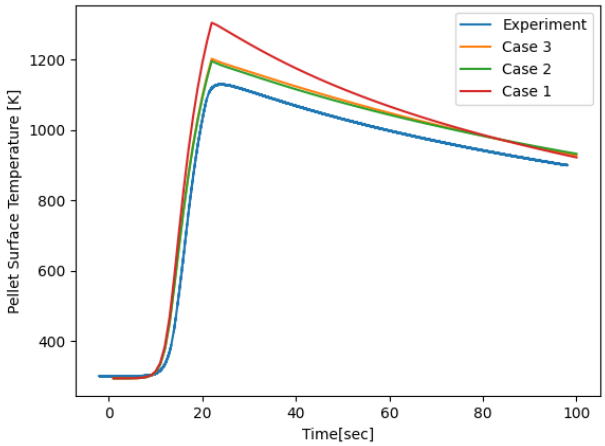

Fig. 14. SIRIUS-3 Outer Center Line Computed and Measured Temperatures

Also further differences could be due to the inconsistency between the calibrations factor's density, material composition, and assumed fission energy deposition to that of the Bison model as will be shown and discussed below.

Moreover, in Figure 15 the labels are the same as those in Figure 14, but temperature measurement location is the outer fuel specimen top. Again, the metals close to the fuel conduct energy away from the pellet during the transient and contribute to the heat transfer after the initial pulse. Despite the number of components Case 3 shows a temperature that is above the measurement temperature and does not match the curve slope of the experiment. This indicates possible cooling mechanisms that are not present or that the Bison FEM should be extended with more components to better capture the heat absorption and cooling. This is shown in Figure 1 and Figure 5 where there are a greater number of different metal components which are in contact with the fuel element specimen. These components have an effect even on the thermal conduction and energy dynamics of the top fuel element specimen temperature.

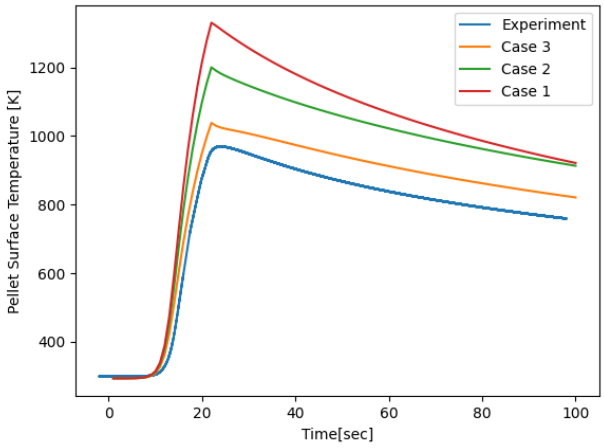

Fig. 15. SIRIUS-3 Top Surface Outer Computed and Measured Temperatures

Furthermore, the effect of different flask emissivities on the outer mid-height temperature are shown in Figure 16, and for these calculations the number of components are given by Case 3 discussed above. As shown in Figure 16 as the flask emissivity increases, the heat radiation emission increases and the mid-height temperature decreases since the fuel element specimen is able to increase heat loss. The result with the emissivity ϵ_2=0.35 is closest to the experimental measurement, and the temperature trend is in alignment with the results shown in Figures 12 and 13. Because the emissivity is much higher than expect of molybdenum, this result indicates that some omitted components such as the standoff rods affect the local radiative transfer than initially expected.

In addition, in Figures 17 and 18 the effects on the pellet FEM surface temperatures from the assumed energy deposition due to fission are shown, and the fuel element specimen density is changed to be consistent with the parameters given

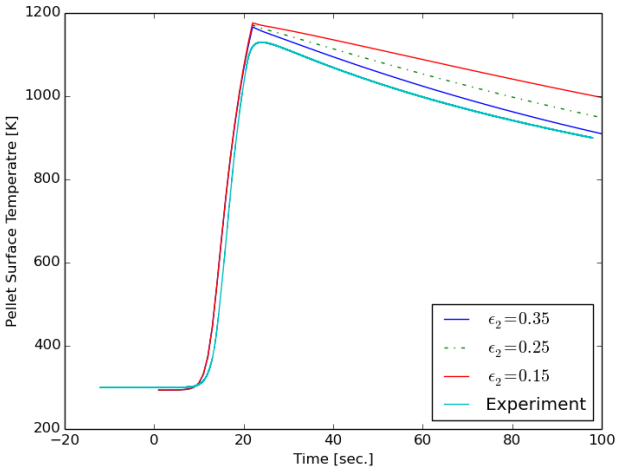

Fig. 16. SIRIUS-3 Outer Mid-Height Computed and Measured Temperatures for Different Flask Emissivities ϵ_2

in reference [7]. In Figure 17 and 18 show that the highest calculated temperatures are the calculations with lower fuel mass or fuel specimen density, and the lowest calculated temperatures are the calculations with calibration factors with 180MeV/fission. Figure 17 and 18 show that Bison FEM with consistent calibration factors and density give results that are closer to measurement.

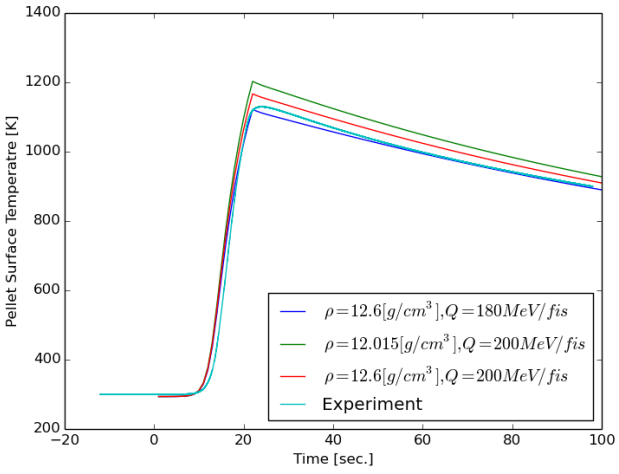

Fig. 17. SIRIUS-3 Outer Mid-Height Computed and Measured Temperatures for different Energy Deposition Coupling Factors

Moreover, in Figure 17 the calculation with the coupling factor with the assumed 180$MeV/fission$ deposition is slightly lower than the measured temperature, and in Figure 18 the calculation with the coupling factor at 180$MeV/fission$ for fission density is still larger than that of the measured temperature. The measured temperature profile in Figure 18 indicates that additional heat loss occurs. The additional heat loss could be due to thermal heating of more metal components

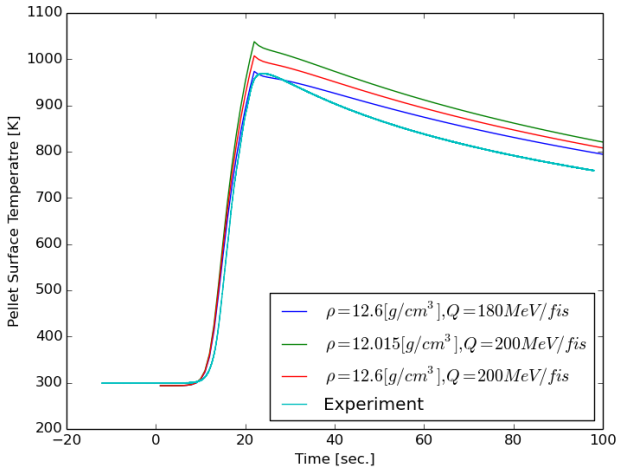

Fig. 18. SIRIUS-3 Outer Top Computed and Measured Temperatures for different Energy Deposition Coupling Factors

than is currently modeled or the establishment of additional heat loss mechanics such as convection that may occur for the top fuel specimens. In Figure 18 the solutions only account for conduction from the top pellet to the retainer cap, and conduction from the retainer cap to the representative hold-down ring. For these cases the hold-down ring is assumed to have radiative heat transfer with the surrounding gas.

VI CONCLUSIONS AND FUTURE WORK

A SIRIUS-3 Bison FEM was developed and compared against the experimental data. Temperatures are calculated that show the same trends or match the measurement data to within $\leq$ 10K depending on the model parameterization and location of the temperature measurement. The BISON FEM helped to deduce the relevant components that must be modeled to obtain an accurate temperature profile. These components included the molybdenum element tubes, the retainer rings and the hold-down ring. From the results, presence or omission of the components is shown to impact the local temperature. For the mid-height temperature the molybdenum element tubes are significant heat sink for the power ramp stage of the transient and also contributes to the cooling behavior of fuel specimen after. For the outer top fuel specimen temperature the molybdenum element tubes, the retainer cap and the hold-down ring all contribute as a heat sinks during the transient and contribute to the cooling to the fuel specimen. The results also show that thermal radiation emission is important in cooling the pellet for the SIRIUS-3 CAL radiation. But the values for the experiment emissivities are uncertain and are not provided. Similar to reference [9], emissivity values are often assigned based on thoughtful judgement of different materials and should be characterized for better modeling of future experiments. Also, other potential heat loss mechanics could be present as shown in the results of the top fuel specimens.

The amount of fission energy assigned was shown to have an impact on the fuel element specimen temperature with a lower coupling factors producing temperatures that match the measured temperatures more accurately. The fuel specimen composition used to calculate the coupling factors should be with consistent material composition and density of the Bison thermal FEM. The consistency would ensure greater accuracy in the calculated temperature results.

In addition, further investigation into dynamic coupling factors could yield better results. As further data becomes available, calculations and comparisons of the Bison FEM should be done to determine the models accuracy. The generation of this knowledge is important for future experiment design of the SIRIUS series.

VII ACKNOWLEDGMENTS

This manuscript has been authored by Battelle Energy Alliance, LLC under Contract No. DE-AC07-05ID14517 with the U.S. Department of Energy, and under this contract was funded by NASA's Space Nuclear Propulsion (SNP) project in the NASA Space Technology Mission Directorate (STMD). The U.S. Government retains and the publisher, by accepting the article for publication, acknowledges that the U.S. Government retains a nonexclusive, paid-up, irrevocable, world-wide license to publish or reproduce the published form of this manuscript, or allow others to do so, for U.S. Government purposes.

This research made use of the resources of the High Performance Computing Center at Idaho National Laboratory, which is supported by the Office of Nuclear Energy of the U.S. Department of Energy and the Nuclear Science User Facilities.

REFERENCES

1. S. K. BOROWSKI, D. R. MCCURDY, and T. W. PACKARD, "Nuclear Thermal Propulsion (NTP): A proven growth technology for human NEO/Mars exploration missions," in "2012 IEEE Aerospace Conference," (2012), pp. 1–20.

2. T. JING, S. SCHUNERT, V. M. LABOURÉ, M. D. DEHART, C.-S. LIN, and J. ORTENSI, "Multiphysics Simulation of the NASA SIRIUS-CAL Fuel Experiment in the Transient Test Reactor Using Griffin," *Energies*, **15**, *17* (2022).
3. F. N. GLEICHER, S. SCHUNERT, M. DEHART, and I. TRIVEDI, "Thermal Modeling and Analysis of the SIRIUS-2 Experiment," in "Transactions of the American Nuclear Society Winter Conference," (2022), pp. 1–5.
4. R. WILLIAMSON, J. HALES, S. NOVASCONE, M. TONKS, D. GASTON, C. PERMANN, D. ANDRS, and R. MARTINEAU, "Multidimensional multiphysics simulation of nuclear fuel behavior," *Journal of Nuclear Materials*, **423**, *1*, 149–163 (2012).
5. C. HILL, "Neutronics Analysis of the NASA SIRIUS-2 Experiment in TREAT," Tech. Rep. ECAR-4886, Idaho National Laboratory (November 2019).
6. J. D. BESS, N. E. WOOLSTENHULME, C. B. JENSEN, J. R. PARRY, and C. M. HILL, "Nuclear characterization of a general-purpose instrumentation and materials testing location in TREAT," *Annals of Nuclear Energy*, **124**, 270–

294 (2019).
7. C. HILL, "Neutronics Analysis of the SIRIUS-3 Experiment in TREAT," Tech. Rep. ECAR-5347, Idaho National Laboratory (2019).
8. N. JARRED, R. SCOTT, and J. ZILLINGER, "Fabrication Control Plan for the Sirius-3 Fuel Elements for Irradiation in TREAT," Tech. Rep. PLN-6334, Idaho National Laboratory (2021).
9. C. HALE, "SIRIUS-3 Thermal Analysis," Tech. Rep. ECAR-5477, Idaho National Laboratory (2019).
10. J. L. MILNER, "Space Nuclear Propulsion Material Property Handbook," Tech. Rep. SNP-HDBK-0008, NASA (2020).
11. J. PETRIE, B. DICKEY, and B. LEGLER, "Radiative and Convective Heat Transfer Within Vertical Annular Spaces Open at the Ends," Tech. Rep. IN 1110, Idaho Nuclear Corporation (1967).
12. J. ORTENSI, B. A. BAKER, M. P. JOHNSON, Y. WANG, V. M. LABOURÉ, S. SCHUNERT, F. N. GLEICHER, and M. D. DEHART, "Validation of the Griffin application for TREAT transient modeling and simulation," *Nuclear Engineering and Design*, **385**, 111478 (2021).
13. J. LAMARSH, *Introduction to Nuclear Reactor Theory*, Addison Wesley Publishing Company Inc. (1966).